Study of axial and transverse surface instabilities in assisted atomization

S. Arnaud, Jean-Philippe Matas, Alain H. Cartellier

Study of axial and transverse surface instabilities in assisted atomization

Sylvain Arnaud, Jean-Philippe Matas and Alain Cartellier

LEGI
38041 Grenoble Cedex 9
E-mail : matas@hmg.inpg.fr

Keywords: atomization, instability, spray formation, passive control

Abstract

Recent studies have shown that assisted atomization depends on the development of two successive instabilities. The mean drop diameter can be predicted as a function of the characteristic lengths of these instabilities. In the first part predictions of the KH model are compared with experiments. A discrepancy is found for low dynamic pressure ratios and/or high liquid velocities. In the second part we investigate a method of passive control of the transverse instability, with metal needles placed on the splitter plate. This method is expected to be relevant at low gas velocity, when atomization is incomplete. Preliminary results show that for a transverse spacing of the obstacles corresponding to the most amplified wavelength, the atomization process is improved in the case of low gas velocities. If however the spacing is larger than the transverse instability wavelength, the performances of the atomization mechanism are degraded.

INTRODUCTION:

Assisted or airblast atomization, in which a liquid jet is atomized by a fast coaxial air stream, is widely used in combustion processes. Applications range from cryotechnic rocket engines to injectors in turboreactors. However, the physical mechanisms causing the transformation of a liquid bulk into droplets have to be better understood in order to improve combustion efficiency and decrease pollutant emissions.

The assisted atomization process is composed of two successive instabilities. The fast air stream causes first a destabilization of the slow liquid stream via a shear instability (similar to a Kelvin-Helmholtz instability, but controlled by the thickness of the gas vorticity layer, Marmottant and Villermaux 2004), and leads to the formation of axial waves. The wave crests next undergo an axial acceleration due to the drag exerted by the air stream: they are then destabilized by a transverse Rayleigh-Taylor instability (Hong et al. 2002, Varga et al. 2003). This causes the formation of ligaments (or fingers), which are swept by the air flow, and finally break into droplets (see Figure 1). Droplet size directly controls combustion efficiency. The nature of the transverse Rayleigh-Taylor instability is still the subject of controversy, a different mechanism having been proposed by Marmottant and Villermaux (2004) in which the acceleration causing the destabilization is perpendicular to the jet (as in a Faraday instability), and not caused by the air drag.

Generic experiments are performed on a two-phase planar mixing layer with strong density and velocity contrasts. The ratio of the dynamic pressures in each phase $M = \rho_L U_L^2/\rho_G U_G^2$ has been shown to be an important parameter: it controls directly the liquid intact length, and consequently the geometry of the two-phase mixing layer (Raynal 1997). As mentioned above, the interface between the liquid and the gas streams first undergoes an axial instability controlled by the thickness of the gas boundary layer. This instability has been studied by a linear stability analysis, and solved for temporal unstable modes. Raynal (1997) has shown that the frequency of the most unstable modes could be approximated by $f_{axi} \propto Uc/\delta_G \propto U_G^{3/2}$, where δ_G is the gas vorticity thickness and U_c is the convective velocity given by a phenomenological model (Dimotakis 1986):

$$U_C = \frac{\rho_G^{1/2} U_G + \rho_L^{1/2} U_L}{\rho_G^{1/2} + \rho_L^{1/2}}. \qquad (1)$$

This result finds its limits when M is below several units (Ben Rayana 2007), the extreme case being the case of a liquid jet injected into a still gas (Hoyt & Taylor 1977). In this case the axial and transverse instabilities have the same characteristic lengths, unlike in assisted atomization where the transverse wavelength is much shorter than the axial one. But what happens for intermediate values of M? In the first part of our study we will try to investigate how the results validated for high M assisted atomization cease to be valid when M is decreased.

The second stage of atomization involves a destabilization of the axial waves by a transverse Rayleigh-Taylor instability. The wavelength of this instability can be expressed as a function of the axial acceleration *a* of the wave, surface tension σ and liquid density ρ_L:

$$\lambda_{RT} = 2\pi\sqrt{\frac{3\sigma}{a\rho_L}}$$

The acceleration can be related to the axial wave size via the drag on the wave and its inertia (Hong 2002, Varga 2003). Marmottant (2004) has shown that drop size is proportional to the transverse wavelength: the model consequently gives D_{10} and D_{32} as direct functions of injection conditions, provided that the parameter M is large enough (Hong et al. 2002, Ben Rayana 2007). The model more precisely states that drop size scales as $D_{10} \propto U_G^{-5/4}$. However a discrepancy was observed for low gas velocities: a different scaling $D_{10} \propto U_G^{-2}$ was measured for U_G < 30m/s. This regime corresponds to a regime where the formation of ligaments is incomplete: the number of formed ligaments is lower than the expected number of ligaments. In the second part we will concentrate on drop formation in this regime of low gas velocities. Our objective is to force the transverse instability and to test the efficiency of this forcing on ligament formation and drop size.

We begin by presenting the experimental set-up in part 2. Part 3 exposes the results of our measurements on the axial instability at low M. Part 4 is dedicated to the influence of a spatial forcing of the instability on particle size. Part 5 is the conclusion.

EXPERIMENTAL FACILITY:

In our case, experiments are performed on a two-phase planar mixing layer. We used water and air in ambient conditions (20°C and atmospheric pressure). Fluid streams are delivered through convergent rectangular cross-section nozzles (figure 1). At the exit of both nozzles, the transverse extension is 10 cm and the height is 1cm (the height in the gas and liquid phase are noted respectively H_G et H_L). With this aspect ratio we neglect the influence of side walls, and ensure that the flow is bidimensional (see Figure 1 and 2). Injection of both fluids is made through honeycombs and with a smooth convergence (contraction ratio is 10), to ensure relatively clean flows where the intensity of perturbation and turbulence is reduced. Air and water mean velocities measurements are made respectively with a mass-flowmeter and a rotameter (Krohne). Air velocity was varied in the range [15m/s ; 35 m/s] and water velocity in the range [0.1 m/s ; 1.1 m/s] corresponding to M in the range [0.8 ; 38] and a gas boundary layer thickness δ_G in the range [400 µm ; 600 µm].

Measurements of the frequency of the axial instability is made by strobe light. Special care is taken to avoid the measurement of harmonic or sub-harmonic frequencies. The method employed is to vary strobe frequency until the waves appear frozen for a given value of U_G and U_L.

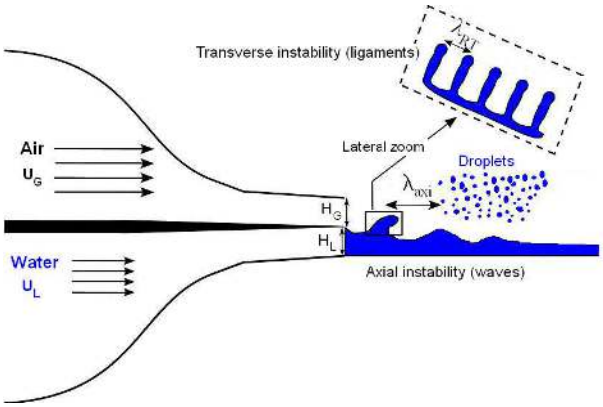

Figure 1 – Sketch of the experimental facility and atomization scenario

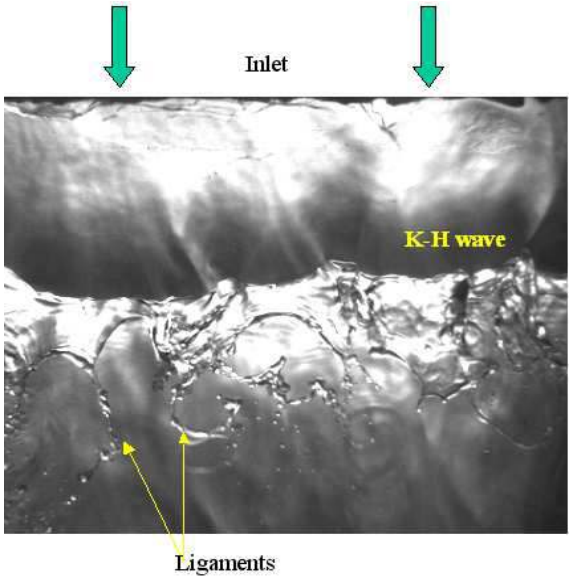

Figure 2 – Visualisation of the flow, width = 7cm U_G=25m/s U_L=0.3m/s M=8.

The transverse instability is studied by visualization with a CCD camera. A spatial forcing is applied on the flow with the use of metal needles : the needles are set on the splitter plate, on the gas side, at a spacing corresponding to the transverse wavelength at a given gas velocity.

Particle size is measured with an optical probe : the optical probe is positioned above the end of the liquid intact length, at the height of the splitter plate. The signal delivered by the probe, once processed, gives for each drop impacting the probe its velocity and chord (Hong et al 2004). Sauter diameter is directly obtained via the mean chord through the relation $d_{32} = (3/2)C_{10}$. The chord distribution can also be inverted to give the diameter distribution, from which the mean diameter d_{10} can be extracted.

STUDY OF THE AXIAL INSTABILITY

As indicated below, the measurements of frequency for the axial Kelvin-Helmholtz instability are made with a stroboscope. The gas velocity U_G is fixed, and liquid velocity U_L is varied in the largest possible range. Figure 3 shows the results obtained for 4 different gas velocities.

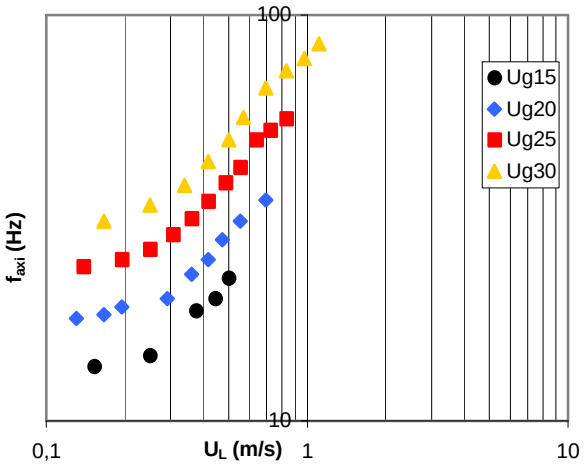

Figure 3 – Axial instability frequency vs. water velocity U_L, for fixed gas velocity U_G.

We can observe two zones: for $U_L < 0.3$m/s there is a weak influence of the liquid velocity U_L on the axial frequency f_{axi} ; for $U_L > 0.3$m/s there is on the contrary a very steep increase of f_{axi} with U_L. As mentioned in the introduction, the model based on KH instability predicts a scaling $f_{axi} \propto Uc/\delta_G$. This scaling is expected to be valid for large M. How do our data compare with this prediction? We plot on figure 4 the ratio $f_{axi}/(Uc/\delta_G)$ as a function of the dynamic pressure ratio M.

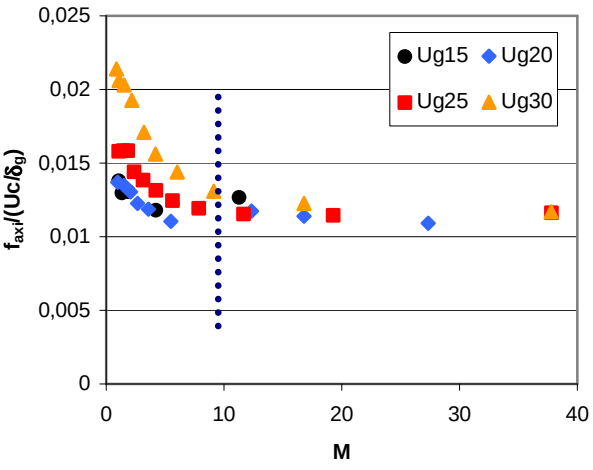

Figure 4 – Axial frequency nondimensionalized by Uc/δ_G, as a function of the dynamic pressure ratio M.

Figure 4 exposes clearly how experimental data deviates from the phenomenological model for M < 10. The scaling is however very good for M > 10, showing that in this regime the model efficiently captures the scaling of the axial frequency. In addition, in this regime the ratio $f_{axi}/(Uc/\delta_G)$ is the same for the four values of gas velocity investigated. For large values of M, the scaling of f_{axi} can be simplified, since in this case according to (1) we have $Uc \propto U_G$: this leads to $f_{axi} \propto U_G^{3/2}$. But this scaling is only valid for large values of M.

For M < 10 the experimental frequency deviates strongly from the frequency predicted by the model. We want to distinguish if this deviation is due to the simplifications introduced in the derivation of the model, or if it is a failure of the linear stability analysis on which the model is based. The dispersion relation obtained from linearization of Navier-Stokes equations plus continuity conditions is given by:

$$e^{-2K} = \frac{\left(2\left(K\frac{r_2}{r_2-1}-\Omega\right)-1\right)\left(K\left(Ri_\delta-\frac{K^2}{We_\delta}\right)+\left(\frac{K}{r_2-1}-\Omega\right)^2\left(1+\frac{1}{S}\right)+\left(\frac{K}{r_2-1}-\Omega\right)\right)}{-K\left(Ri_\delta-\frac{K^2}{We_\delta}\right)+\left(\frac{K}{r_2-1}-\Omega\right)^2\left(1-\frac{1}{S}\right)-\left(\frac{K}{r_2-1}-\Omega\right)}$$

with $r_2 = U_G/U_L$ the velocity ratio, $S = \rho_G/\rho_L$ the density ratio, $\Omega = \omega\delta_G/(U_G-U_L)$ the nondimensionalized pulsation, and $K = k\delta_G$ the nondimensionalized wavenumber. This dispersion relation also takes into account possible gravity effects and capillarity effects via the Richardson and Weber numbers based on δ_G:

$$Ri_\delta = \frac{(\rho_L-\rho_G)g\delta_G}{\rho_G(U_G-U_L)^2}, \quad We_\delta = \frac{\rho_G(U_G-U_L)^2\delta_G}{\sigma}.$$

The velocity profile in the boundary layer is assumed to be linear, and the boundary layer in the liquid is not taken into account (figure 5a). Even though this profile is markedly different from the experimental velocity profile (figure 5b), we follow Raynal (1997) in assuming that these differences do not affect quantitatively the results of the stability analysis. The dispersion relation is solved with Matlab for values of U_G and U_L corresponding to the experimental ones. We look for spatially unstable solutions, given the a priori better agreement of experimental conditions with a spatial analysis than with a temporal analysis.

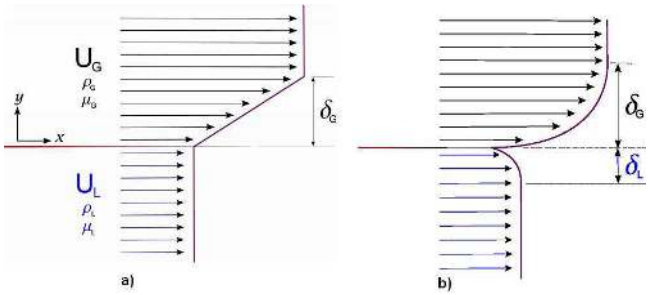

Figure 5 – Raynal's linear stability (a) and real (b) inlet velocity profiles

For given flow conditions, the solver yields a region of positive K_i (imaginary part of the nondimensionalized wave

number), corresponding to spatially unstable solutions (see for example figure 6, with values at U_G = 30 m/s). We extract from these curves the value corresponding to the most unstable mode. Figure 6 shows that the frequency of the most unstable mode increases with increasing U_L , in accordance with the trend observed in experiments.

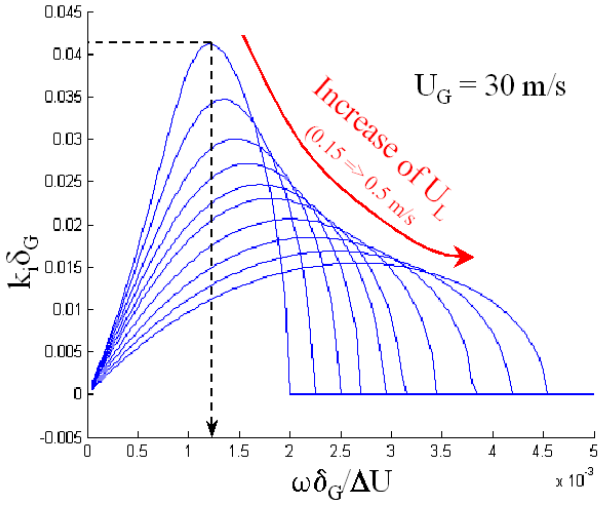

Figure 6 – Growing rates K-H instability

In order to quantitatively compare experiments and the results of spatial theory, we plot on figure 7 the ratio of the experimental frequency to the frequency of the most unstable spatial mode. Even though there is still a deviation at low M, the regime where the experimental frequency is captured is extended to M>7. In addition, the magnitude of deviations for low M appears to be relatively lower than when the frequency is scaled by Uc/δ_G (compare low M regions for figure 4 and for figure 7). There is however a clear failure of the spatial theory, as in the case scaling by Uc/δ_G, for low M and large values of the gas velocity. For low values of M but low values of U_G (U_G = 15 m/s and U_G = 20 m/s), the deviation is almost non-existent.

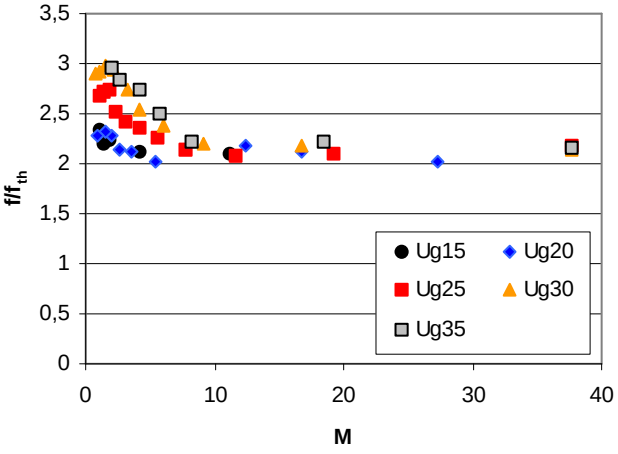

Figure 7 – Ration of measured axial and theoretical frequency as a function of M. Experimental data is well captured by theory for large M.

This large dispersion of data for low values of M suggests that M may not be the right parameter in this domain. We plot the same data on figure 8, but this time as a function of $1/U_L^2$ (in order to allow comparison with figure 7). It can be seen on figure 8 that the data for low M, or equivalently for large liquid velocities, now roughly collapse on a single curve.

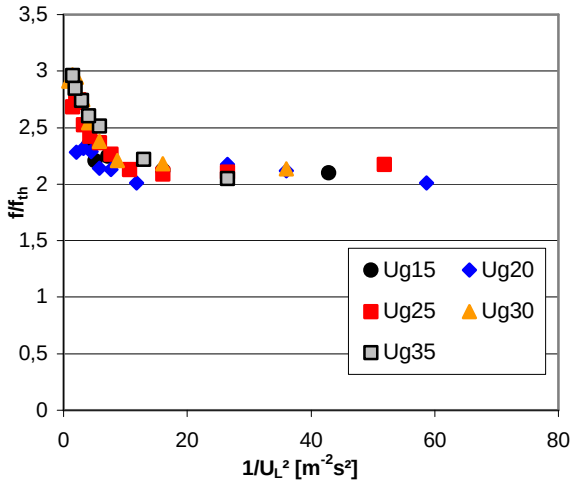

Figure 8 – Ration of measured axial and theoretical frequency as a function of $1/U_L^2$. Curves for different gas velocities are collapsed at low M.

This proves that the failure of the spatial theory is controlled by liquid velocity. What is the physical reason of this failure? Three causes could a priori be responsible for the deviation. The first cause is the influence of the liquid boundary layer δ_L: in the spatial analysis presented above this boundary layer has not been considered. Raynal (1997) has shown that the instability controlled by δ_L had actually a larger growth rate than the instability controlled by δ_G, but that the low Reynolds number of the liquid boundary layer strongly inhibited the growth of this mode. The failure observed on figure 8 for large liquid velocity might then be related to an increase in the Reynolds number of the liquid boundary layer, and consequently an increasing influence of the liquid unstable mode on the gas mode.

The second limitation related to liquid velocity is apparent on figure 5b: the splitter plate induces a velocity deficit in the liquid phase. The time needed to compensate this deficit is expected to depend on U_L. If the deficit is compensated by viscous diffusion, it will decrease in a time $\tau_L \approx \delta_L^2/\nu_L$ (diffusive viscous time). However $\delta_L \propto U_L^{-1/2}$ shows that $\tau_L \propto U_L^{-1}$: for large liquid velocities the time needed to compensate the deficit decreases. The velocity deficit is therefore expected to be a problem for low liquid velocities, and not for large liquid velocities. We can then a priori discard the velocity deficit as a possible explanation for the discrepancy at large U_L.

A final limitation of the spatial theory is due to the neglect of viscosity effects ; the difference of viscosity between the gas and liquid phase can trigger an unstable mode, known as H-mode (Hinch 1984). Recent direct computations of 2D two phase flow have indicated that this mode could be the dominant unstable mode, with

growth rates larger than the inviscid KH-mode (Boeck and Zaleski 2005). This H-mode also exhibits shorter wavelengths in the temporal analysis of Boeck and Zaleski (2005), corresponding to higher frequencies. The deviation observed for large liquid velocities could be caused by the emergence of this mode, even though additional information on the behaviour of the H-mode with liquid velocity would be needed to conclude.

In order to shed light on this issue, we tried to image the flow for conditions of large liquid velocities, and to identify a different behaviour for these conditions. Figure 9 shows a top view of the flow for large U_L (flow is from top to bottom): it can be seen that the flow has lost its two-dimensionality (compare with figure 2), with waves having a lateral extent of the order of their wavelength. It must be noted that this phenomenon coincides with the birth of new ripple-like waves, of very small wavelength (see figure 9); these waves could be parasitic waves (Longuet-Higgins 1962) generated at the crest of the Kelvin-Helmholtz waves, and developing downstream.

In these conditions, where waves have a 3-D structure, measurements of frequency with the stroboscope become impossible. Alternative measurements with a fast camera and/or with an optical probe will be tested soon.

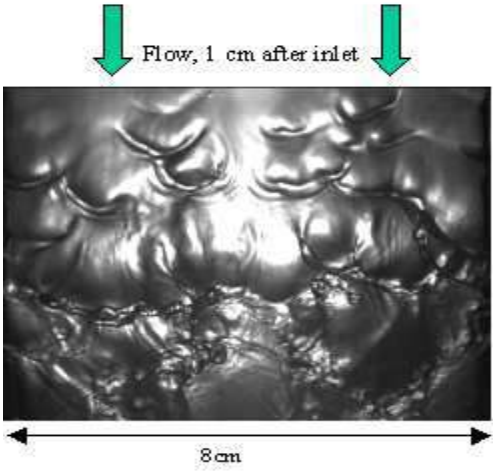

Figure 9 - U_G=20m/s , U_L=0.85m/s, M=0.6

TRANSVERSE INSTABILITY : PASSIVE CONTROL AND PRELIMINARY RESULTS

We will now focus on the transverse instability. The dynamic pressure ratio M is fixed to a constant value. Since the liquid intact length is directly controlled by M, this warrants that measurements are made for a fixed intact length, i.e. for a fixed two-phase flow geometry. In order to compare our results with those of Ben Rayana (2007), we choose to work at M = 16.

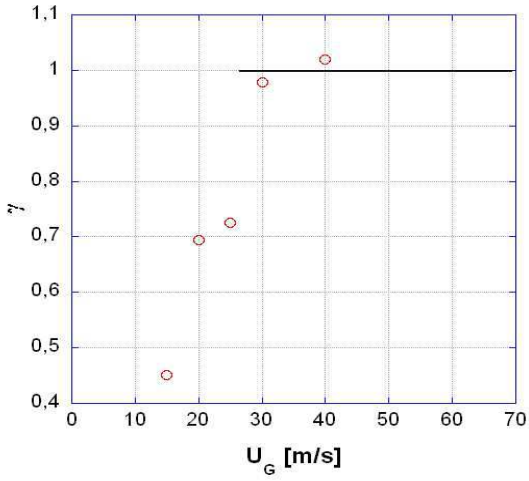

Figure 10 - Dimensionless ligaments lineic density as a function of the gas velocity, M=16 (Rayana et al 2006)

As said in the introduction, for low gas velocities the number of ligaments is lower than expected (U_G < 30m/s at M=16). Figure 10 shows that the lineic density of ligaments decreases for U_G < 30m/s and M = 16 (Ben Rayana et al 2006). We now offer a possible explanation for this phenomenon: In the "classical" transverse instability mechanism, a wave first undergoes an axial acceleration which initiates corrugations on the crest of the wave, spaced at the amplified wavelength of the Rayleigh-Taylor instability. Then, these corrugations are stretched into ligaments. However, one can imagine that ligaments which are not sufficiently developed can drain into their neighbours because of surface tension. Only the remaining, larger, ligaments will then break into droplets.

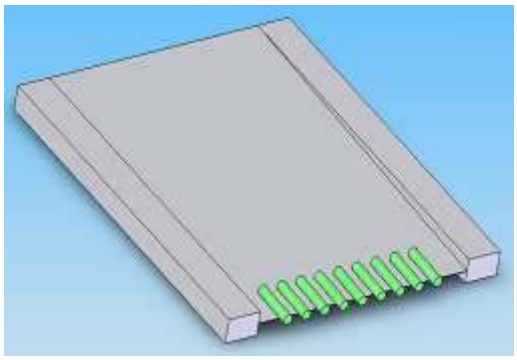

Figure 11 – Splitter plate with obstacles. Metal needles are not to scale.

This possible scenario led us to set up a transverse forcing in order to develop all expected ligaments for gas velocities ranging from 15m/s to 30m/s. The idea is to create an initial deformation of the wave crest at a transverse spacing corresponding to the largest growth rate of R-T instability, therefore helping ligament formation. To achieve this, we force a perturbation with obstacles glued at the end of the splitter plate (see figure 11).

Several types of obstacles have been tested. Preliminary measurements via visualization, and ligament lineic density λ_{RT}^{-1} counting (over a set of 100 images),

suggested that metal needles were the most efficient in increasing the number of ligaments per wave (about 10%). Larger obstacles were also tested: their wake and interaction with the fluid phase were so important that they drastically changed the flow structure (see figure 12) making any counting of ligament quite arduous.

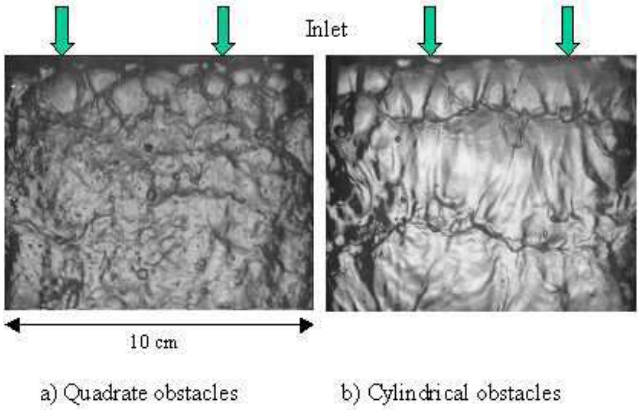

Figure 12 – Large obstacles (characteristic length 4mm) U_G=18m/s , M=16.

The metal needles are 0.8mm in diameter and 15mm long. We place them at a transverse spacing corresponding to $\lambda_{RT} = U_G^{-5/4}\sigma^{1/2}$ (Hong 2002). The needles are set so as to project 3mm beyond the splitter plate (figures 11 and 13). Thus, they create a transverse gas velocity modulation and an initial perturbation of the interface. The meniscus created by each needle can be distinguished on figure 13.

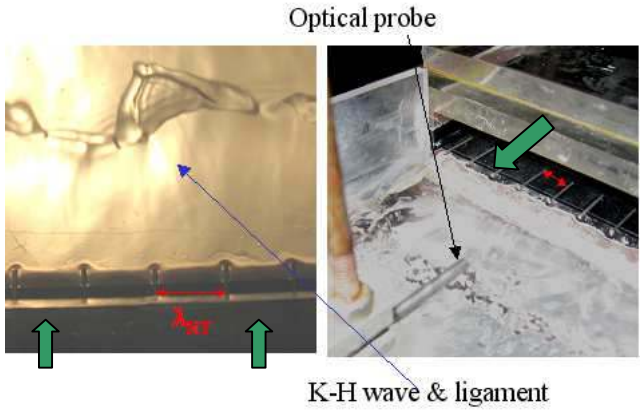

Figure 13 – Splitter plate with metal needles. U_G=15m/s, M=16, λ_{RT}=9mm

We carried out two types of measurements with the optical probe: firstly, we adapted the transverse spacing for each gas velocities (λ_{RT} ranging from 4.8mm to 9.1mm, corresponding to the range U_G=25m/s to 15m/s) and observed the behaviour of the spray distribution characteristics. Secondly, measurements were made with λ_{RT} constant equal to 7.2mm (corresponding to U_G=18m/s). The spatial position of the optical probe is kept constant, at the end of the intact liquid length.

To obtain accurate properties of the spray, we need to calibrate the optical probe. This step was made difficult by the use of a new type of optical fiber, exhibiting a different behaviour than optical probes previously used with the same set-up. This is why, in the following, we only present qualitative results when comparing the forced situation with the unforced case.

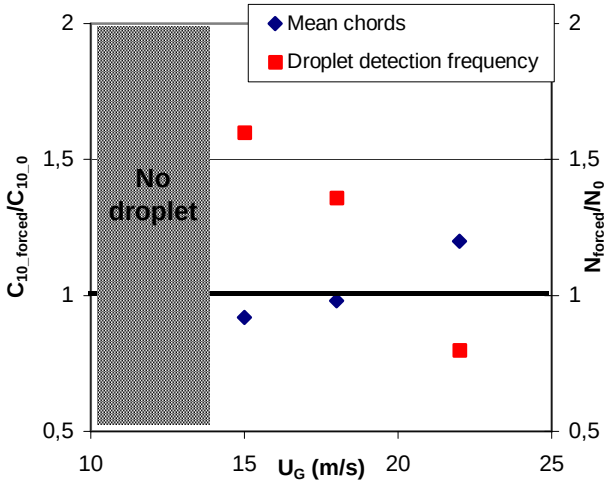

Figure 14 – Optical probe measurements for a forcing at a transverse wavelength adapted to each gas velocity, for M=16. Comparison of the ratio of mean chord in forced case to mean chord in unforced case (blue symbols) ; ratio of droplet detection frequency in forced case to unforced cases (red symbols).

We can firstly observe that metal needles have an effect on atomization. Indeed, the droplet detection frequency N is increased for gas velocities between 15 and 20m/s (figure 14). In parallel, the mean chord C_{10} seems to be less affected by the control, with only a weak increase of the ratio $C_{10\ forced}/C_{10\ unforced}$ when U_G is increased. These preliminary results consequently indicate that the forcing is effective in increasing the quality of atomization. However, for higher gas velocities, the mean chord is larger in the forced case than in the unforced case, and the number of detected drops is simultaneously lower (figure 14 for U_G > 20 m/s). This corresponds to a ratio γ close to 1 (see figure 10), i.e. a number of formed ligaments close to the number of expected ligaments. In these conditions, the forcing is unable to improve the quality of atomization, and even appears to degrade it. Further data is needed to confirm these results. High-speed camera visualization could also help us describe the flow structure.

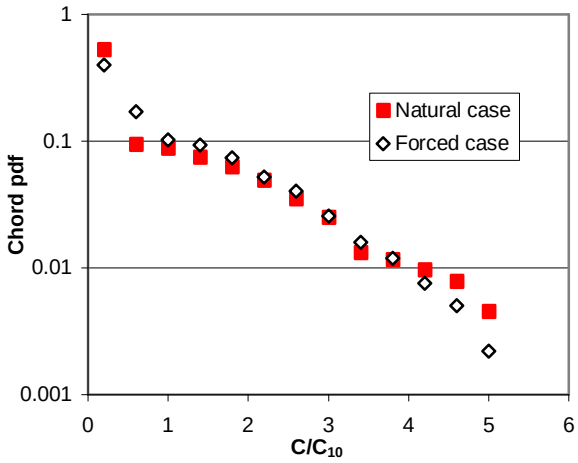

Figure 15 – Chord distribution for U_G=18m/s, M=16

Figure 15 shows the chord distributions obtained after the optical probe signal is processed for U_G=18m/s, in the forced case and in the unforced case. Figure 15 shows that the chord distribution is roughly the same between the natural and the forced case in this regime, in accordance with the data of figure 14. It can be noted that the unforced case exhibits a slightly broader distribution. The numeric flux φ can be estimated as $\varphi = N/D_{20}$, a relationship valid in the case of uncorrelated radii and velocities (Hong 2002). This gives a numeric flux of $2.5.10^{-5}$ #/m^{2}s in the unforced case, and a slightly larger value of 3.10^{-5} #/m^{2}s in the forced case: the variation is of the order of $(\varphi_{forcing}-\varphi_0)/\varphi_0$ =20%.

We now present results obtained for a fixed spacing of the needles not corresponding to the gas velocity investigated. We take a value of 7.2mm, corresponding to the transverse wavelength at a gas velocity U_G = 18 m/s. Figure 16 shows the chord distribution obtained for the unforced case, and for the forced cases at U_G=30m/s. Two locations of measurements are chosen in the forced case: in front of a metal needle and between two metal needles. It can be seen that larger chords are observed for measurements in front of the needles. A larger mean chord is observed for these conditions, confirming this result.

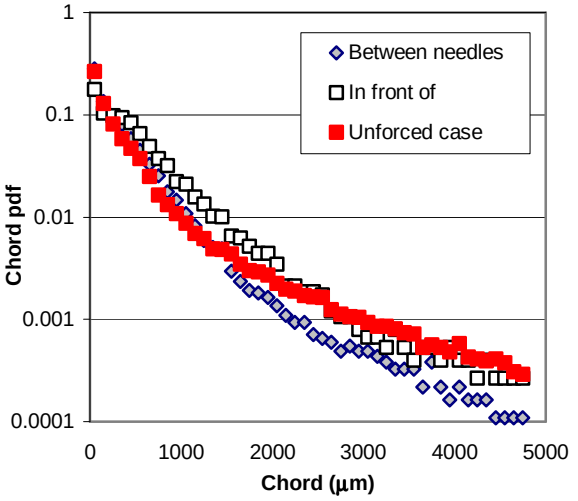

Figure 16 – Chord distribution for U_G=30m/s. With and without forcing at λ_{RT}=7.2mm.

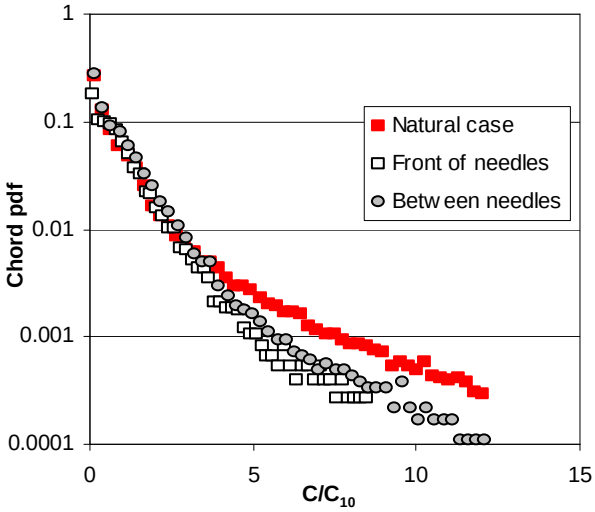

Figure 17 – Dimensionless chord distribution for U_G=30m/s. With and without forcing at λ_{RT}=7.2mm.

Figure 17 now shows the chord distributions this time as a function of the ratio C/C_{10}. The chord distributions for smaller chords (most probable values) are now nearly similar in the natural case or with forcing, contrary to the case of figure 16.

We could observe that when the forcing is not adapted, the numeric flux is smaller than in the natural case. The loss of flux is well-marked when the optical probe is positioned in front of a metal needle. When the probe is positioned between two needles, the flow might have enough space to develop naturally for these conditions. Effectively, the transverse wavelength corresponding to U_G = 30 m/s is 3.8 mm, twice as small as the spacing between needles.

Our results show that a non-adapted forcing (forcing at a larger wavelength) degrades strongly the atomization process. This degradation, as well as the enhancement of atomization observed when forcing is adapted, need to be further investigated.

CONCLUSION:

We have studied two successive instabilities which lead a liquid jet to break into droplets when it is sheared by a fast air stream.

For the axial instability (Kelvin-Helmholtz type), experimental measurements of the frequency show that the phenomenological model proposed by Ben Rayana 2006 finds its limit for M≈10. Going back to the original linear stability analysis from which the model was built limits the extent of the discrepancies with experiments. However, significantly larger frequencies than predicted are observed for large liquid velocities. The exact role of the liquid phase on the instability (via its boundary layer or via a viscous mode) has to be understood before further progress can be made.

In the second part, we proposed a passive control method with metal needles on the splitter plate to increase ligament production at low gas velocities. The aim is to force the transverse instability (Rayleigh-Taylor type)

which transforms waves into ligaments. Preliminary results give an increase of numerical droplet flux for a forcing at the most amplified wavelength, and a decrease of mean chord for low gas velocities. However, forcing at a larger wavelength than the natural one seems to impair atomization. More measurements are needed to confirm this result. Visualization with a fast camera could also help us determine how the flow structure and the spray characteristics are impacted by the forcing.

REFERENCES:

Ben Rayana, F., Cartellier, A. and Hopfinger,E.J., Assisted atomization of a liquid layer : investigation of the parameters affecting the mean drop size prediction. *ICLASS*, Kyoto 2006

Ben Rayana, F. Contribution à l'étude des instabilités interfaciales liquide-gaz en atomisation assistée et tailles de gouttes, PhD Thesis, UJF Grenoble France 2007

Boeck, T. and Zaleski, S. Viscous vs. inviscid instability of two phase mixing layers with continuous velocity profile. *Phys. Fluids.*, **17.** 2005

Dimotakis, P.E. Two-dimensional shear layer entrainment. *AIAA*, 1986

Hinch, E. A note on the mechanism of the instability at the interface between two fluids. *J. Fluid Mech*., **144** 1984

Hong, M., Cartellier A. & Hopfinger E.J., Atomization and mixing in coaxial injection. *Proc 4th Int Conf on Launcher Technology*, Liège Belgium 2002

Hong M., Cartellier A. & Hopfinger E.J., Characterization of phase detection optical probes for the measurement of the dispersed phase parameters in sprays, *Int. J. Multiphase Flow*, **30** 615-648 (2004)

Hoyt, J.W. and Taylor, J. Waves on water jet. *J. Fluid. Mech.* **83,** 1977

Lasheras, J.C., and Hopfinger, E. J. Liquid Jet instability and atomization in a coaxial gas stream. *Annu. Rev. Fluid Mech.*, **32**, 275-308, 2000

Longuet-Higgins, M.S. The generation of capillary waves by steep gravity waves. *National Institute of Oceanography*. 1962

Marmottant, P and E. Villermaux. On spray formation. *J. Fluid Mech.*, **498**, 2004

Raynal, L. Instabilité et entraînement à l'interface d'une couche de mélange liquide-gaz.: PhD Thesis, UJF Grenoble France 1997.

Varga, C.M., Lasheras, J.C. and Hopfinger, E.J., Initial break-up of a small-diameter liquid jet by a high-speed gas stream, *J. Fluid Mech.*, **497**, 2003.